NASA Technical Memorandum 107015

# Numerical Simulation of Heat and Mass Transport During Space Crystal Growth With MEPHISTO

Minwu Yao
*Ohio Aerospace Institute*
*Cleveland, Ohio*

Raghu Raman
*University of Florida*
*Gainesville, Florida*

and

Henry C. de Groh III
*Lewis Research Center*
*Cleveland, Ohio*

July 1995

National Aeronautics and
Space Administration

# NUMERICAL SIMULATION OF HEAT AND MASS TRANSPORT DURING SPACE CRYSTAL GROWTH WITH MEPHISTO

Minwu Yao
Ohio Aerospace Institute, Brook Park, OH 44142

Raghu Raman
University of Florida, Gainesville, FL 32611

Henry C. de Groh III
NASA Lewis Research Center, MS 105-1, Cleveland, OH 44135

## ABSTRACT

The MEPHISTO space experiments are collaborative United States and French investigations aimed at understanding the fundamentals of crystal growth. Microgravity experiments were conducted aboard the USMP-1 and -2 missions on STS-52 and 62 in October 1992 and March 1994 respectively. MEPHISTO is a French designed and built Bridgman type furnace which uses the Seebeck technique to monitor the solid/liquid interface temperature and Peltier pulsing to mark the location and shape of the solid/liquid interface.

In this paper the Bridgman growth of Sn-Bi and Bi-Sn under terrestrial and microgravity conditions is modeled using the finite element code, FIDAP*. The numerical model considers fully coupled heat and mass transport, fluid motion and solid/liquid phase changes in the crystal growth process. The primary goals of this work are: to provide a quantitative study of the thermal buoyancy-induced convection in the melt for the two flight experiments; to compare the vertical and horizontal growth configurations and systematically evaluate the effects of various gravity levels on the solute segregation. Numerical results of the vertical and horizontal Bridgman growth configurations are presented.

---

* NASA does not endorse commercial products. Details about the products named in this paper were included for completeness and accuracy. No endorsement or criticism of these products by NASA should be assumed.

## 1. INTRODUCTION

The low gravity ($g$) environment of space has the potential to produce conditions in which buoyancy-driven convection is suppressed. This convection-free environment can then be used to examine the influence of convection on various phenomena. Of significant interest to industry and the scientific community is how convection influences solidification processes. This interest is due to the complex relationship among thermal conditions, thermal and solutal convection, growth morphology, and macrosegregation in solidified alloy ingots and sensitive electronic materials [1,2]. Direct, quantitative analysis of convection in molten metals and semiconductors is particularly difficult. These materials are generally opaque, which hinders non-intrusive measurements. Furthermore, the chemical volatility of the melt makes the insertion of thermocouples impractical. Thus, most studies are limited to indirect measurement techniques such as temperature and Seebeck measurements, Peltier pulsing and post-mortem analysis. The role of numerical modeling then becomes crucial in analyzing the system. A better understanding of how convection influences solidification can be achieved through synergistic numerical [3] and analytical modeling in combination with various solidification experiments on earth [4,5] and in space.

MEPHISTO [6] is a collaborative effort among Dr. R. Abbaschian (Univ. of Florida at Gainesville), Dr. J.J. Favier and teams from Centre d'Etudes Nucleaires de Grenoble (CENG) and Centre National d'Etudes Spatiales (CNES) in France, and NASA. The MEPHISTO furnace was designed and built by the French teams and solidifies three samples simultaneously in a Bridgman type arrangement. The French team examined the non-faceted solidification of Sn-Bi alloys in the first flight of MEPHISTO. In the second flight of MEPHISTO the faceted growth of the semi-metal Bi (alloyed with a small amount of Sn) was studied. The furnace uses the Seebeck technique in one of the samples to measure the temperature of the solid/liquid (s/l) interface, Peltier pulsing to mark the shape of the interface in the second sample, and has quench capabilities which enable the solute profile in the liquid in front of the interface to be determined in the third ingot. During flight, all pertinent aspects of MEPHISTO are monitored and controlled through the Payload Operations Control Center (POCC), at NASA's Marshall Space Flight Center, enabling repeated melting and solidification runs to be performed at a variety of growth rates. As shown in Figure 1, the MEPHISTO furnace is located during flight on an experiment bridge known as MPESS (the Mission-Particular Equipment Support Structure) in the Shuttle's cargo bay. Goals of the MEPHISTO experiments include determination of how convection influences: a) morphological stability of the s/l interface and the resulting segregation patterns, and b) atomic attachment kinetics at the freezing interface, measured in part from the growth rate and undercooling measurements.

An important part of analyzing processes in space is a full understanding and appreciation for the residual gravity present, both quasi steady and transient ($g$-jitter) [7-10]. For example, during MEPHISTO 2 the Shuttle was flown in the -ZLV, +YVV attitude, which is with the cargo bay toward the Earth and the right (starboard) wing into the velocity vector; and in the -XLV, -ZVV attitude, which is with the Shuttle's tail to the Earth and the cargo bay into the velocity vector. These

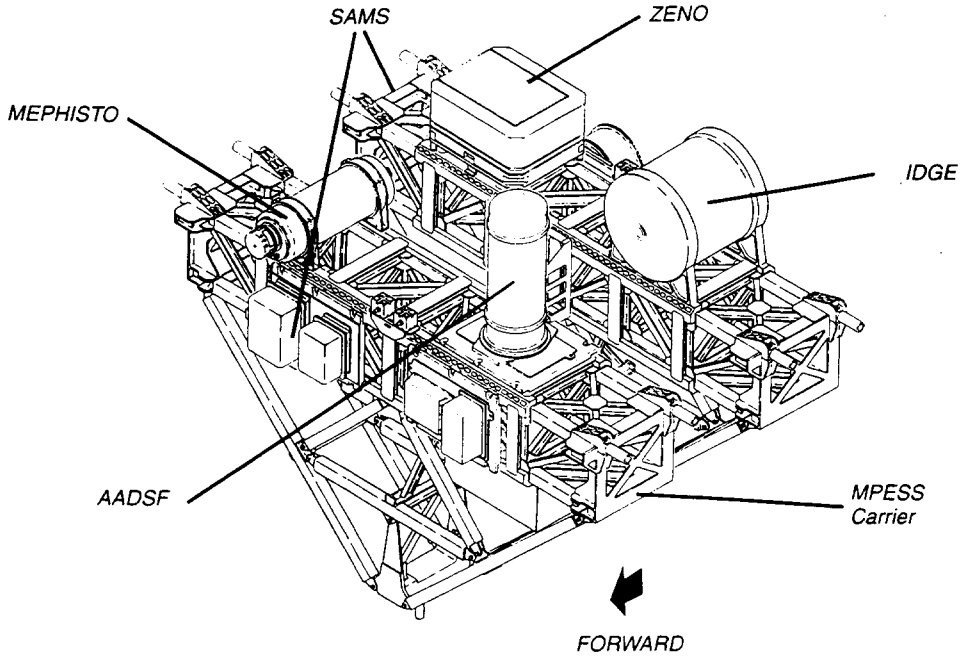


**Figure 1.** Showing the MPESS carrier, which is located in the Shuttle's cargo bay, and USMP- 2 experiment hardwares: MEPHISTO, Advanced Automated Directional Solidification Furnace, the Critical Fluid Light Scattering Experiment known as ZENO, Isothermal Dendrite Growth Experiments, and Space Acceleration Measurement System.

two modes of flight will result in residual gravities of different magnitudes and directions. G-jitter is generally assumed to be independent of Orbiter orientation and is measured using SAMS (Space Acceleration Measurement System). Steady state residual $g$ can be considered in two parts, i.e. drag and tidal acceleration. The $g$ due to aerodynamic drag is always parallel to the velocity of the Shuttle and can be estimated from values in the literature which are sensitive to Shuttle orientation (frontal surface area) and altitude [7,12]. Tidal accelerations are comprised of rotational or centrifugal forces and gravity-gradient contributions [7,9]. Tidal forces vary proportionally with distance from the center of mass (CM) of the Shuttle, and are weakly influenced by orbit altitude. Centrifugal forces enhance the gravity-gradient acceleration in the local vertical direction, making tidal g greater (per unit length) in the direction along the radius of the Earth. The centrifugal force cancels the gravity-gradient force in the flight direction. Thus the tidal residual gravity contribution is zero in the direction of the Shuttle's velocity vector, making drag and tidal forces always perpendicular. This is significant because, unless an experiment is located at CM, the vector sum of tidal and drag forces is always at an angle (other than 0 or 90°) to the velocity vector, making it nearly impossible to align the steady state residual $g$ vector with the axis of the experiment sample. In addition, the location of an experiment in the cargo bay is not usually known until very late in the flight project's schedule. Thus steady residual $g$ can not usually be considered productively in the design

of the experiment hardware. The MEPHISTO furnace on STS-62 was located at approximately (x,y,z) = (24,1.05,10.8) meters, with CM at approximately (x,y,z) = (27.7,0,9.4) meters. With these locations and literature data [7,12] the tidal forces can be estimated and then summed with the drag to determine the total residual steady $g$ and its direction. In this work we examine numerically the effects of these quasi-steady accelerations. The detrimental effects of $g$-jitter were found to be greater than those due to drag and tidal accelerations during MEPHISTO 1. A comparison of the quasi-steady and $g$-jitter forces is provided elsewhere [12]. Numerical examination of $g$-jitter and Bridgman solidification will be dealt with in a later paper.

Theoretical work presently being done in support of MEPHISTO includes the examination of scaling laws, analytical modeling, and parametric experimental studies [13-23]. Our simulations are being used to determine the thermal, solutal and flow fields, and to check the validity, extension and generalization of the scaling laws developed. Similar numerical techniques are being used to examine other space experiments [23] such as the gallium arsenide crystal growth in microgravity experiment [24].

In this paper, we report the recent progress in our ongoing numerical modeling in support of the MEPHISTO experiments. Our main objectives are: to provide a quantitative study of the thermal buoyancy-induced convection in the melt for the two MEPHISTO space experiments; to compare the vertical and horizontal growth configurations; and systematically evaluate the effects of various gravity levels on the solute segregation. Two basic growth configurations are examined in this work: one with the residual gravity vector parallel to the ampoule axis and the second with the residual $g$ perpendicular to the ampoule axis. Calculation of the solute field was included in our analysis of MEPHISTO 1 but was omitted from our simulations of MEPHISTO 2. And although we have solved for interface shape, our presentation of these preliminary results will concentrate on the global fluid flow and the likely effects of this flow on macrosegregation.

## 2. MEPHISTO GROUND AND SPACE EXPERIMENTS

All MEPHISTO ground and space experiments have used Bridgman type furnaces with an isothermal hot zone, an insulated gradient zone, and an isothermal chill zone. The MEPHISTO furnace was designed and built by the French teams and solidifies three samples simultaneously in a dual opposed Bridgman type arrangement. Figure 2 shows a schematic of the flight hardware and the thermal gradient imposed. The ground (1-$g$) experiments were done using the engineering and flight MEPHISTO furnace duplicates located in France and in similar Bridgman furnaces at the University of Florida. All experiments done in France were in the horizontal orientation, with both vertical and horizontal Bridgman experiments being performed at the University of Florida.

All experiments used fused silica ampoules with a 10 mm outer diameter and 6 mm inner diameter. Ingots of Sn-0.5at%Bi for MEPHISTO 1 and Bi-0.1at%Sn for MEPHISTO 2 were used during flight and in our simulations. The pertinent physical properties for silica, Bi, and Sn are tabulated in Table 1 in the Appendix. Some of the values in Table 1 are a result of our

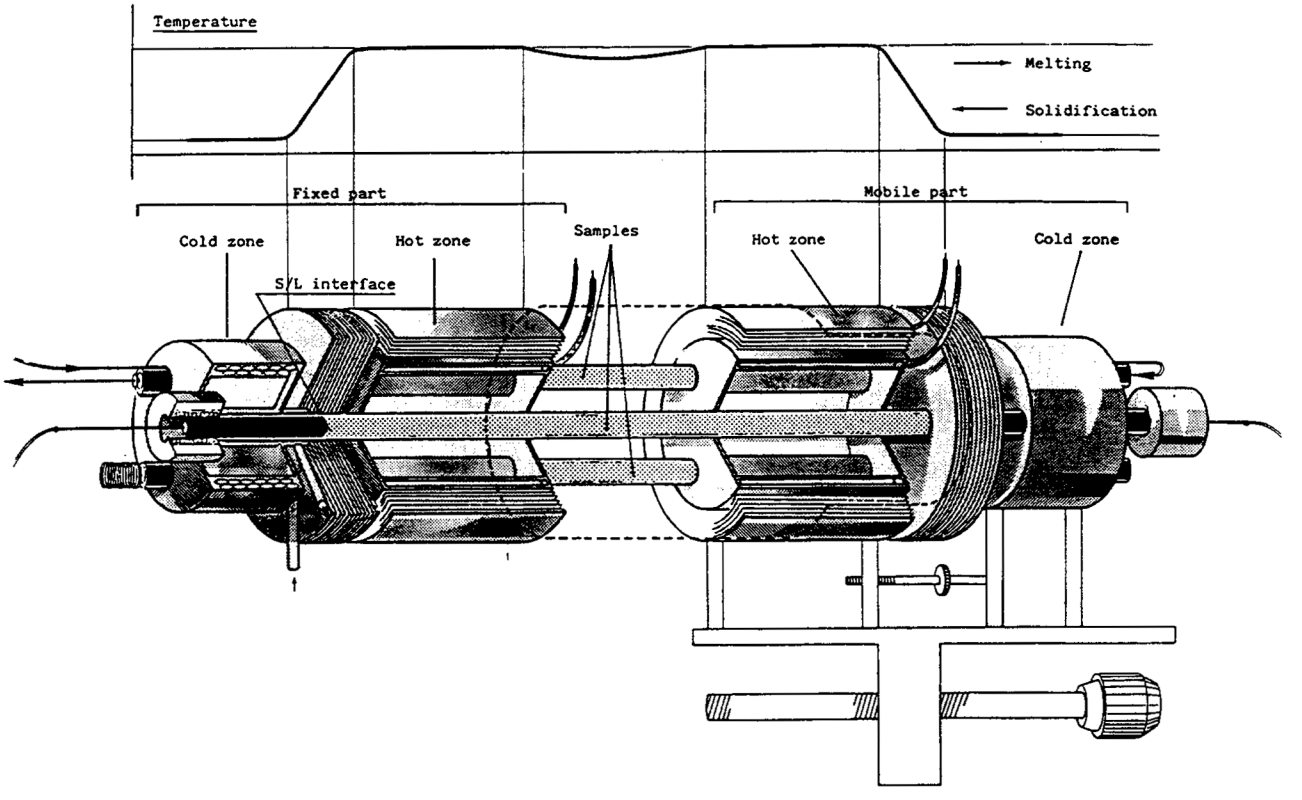


**Figure 2.** Schematic of MEPHISTO furnace and sample temperature profile.

own distillation of several sources in an effort to obtain more accurate properties over a wider temperature range.

Solidification growth speeds in the ground based experiments ranged from 3.6 to 1800 mm/hr, and measured thermal gradients at the s/l interface from 90 to 214 K/cm. During flight, growth speeds varied from about 6 to 170 mm/hr with thermal gradients of approximately 200 K/cm in the liquid. The thermal gradients imposed along the ampoule wall depend on the temperatures of the hot and cold zones and the longitudinal length of the insulated (adiabatic) zone. Information regarding the hot and cold zone temperatures and the length of adiabatic zone used in the ground based and flight experiments are listed in Table 2 in Appendix. Of critical importance in numerical modeling efforts is the accuracy of the input boundary conditions. In this work, the temperatures of the outer surface of the ampoule are used as input boundary conditions. However, complete experimentally measured temperatures were not available along the length of either the furnace or ampoule. The temperatures along the length of the furnace and chill were measured using thermocouples; and, ground based MEPHISTO experiments have shown the ampoule surface temperature to be equal to the furnace (and chill) temperature at locations away from the gradient region. However, an accurate measure of the furnace and ampoule temperature through the adiabatic zone was not available, thus the temperature in the gradient zone between the hot and cold zones was calculated using a zero radial heat loss condition from the adiabatic zone. Also, in the experiments, the isothermal condition

of the hot and cold zones near the adiabatic zone could not be practically maintained due to local heat loss at the zone boundaries. To achieve a smoother, more characteristic longitudinal input temperature profile, the length of the adiabatic zone was adjusted in the model to give a realistic (experimentally verified) temperature gradient in the liquid.

## 3. MATHEMATICAL MODEL

In this paper, we consider heat and mass transport, fluid motion and solid/liquid phase changes in the crystal growth process. In particular, the constitutive property of the melt is assumed to be Newtonian and its motion is described by the following Navier-Stokes equation:

$$\rho_0\left(\frac{\partial \mathbf{u}}{\partial t}+\mathbf{u}\cdot\nabla\mathbf{u}\right)=-\nabla p+\nabla\cdot[\mu(\nabla\mathbf{u}+(\nabla\mathbf{u})^T)]+\rho_0\mathbf{g}[1-\beta_t(T-T_0)] \tag{1}$$

where $\mathbf{u}$ is the velocity vector, $\rho_0$ is fluid density at the reference temperature $T_0$, $p$ is pressure, $\mu$ is viscosity, $T$ is the temperature variable, $\mathbf{g}$ is the acceleration of gravity, $\beta_t$ is the volumetric expansion coefficient, and the Boussinesq model is adopted to approximate the buoyancy force caused by density variation with temperature. Here the change in density associated with species concentration has been neglected. The incompressibility condition is given by

$$\nabla\cdot\mathbf{u}=0\,. \tag{2}$$

The heat transport is controlled by the balance of thermal energy

$$\rho_0 c_p\left(\frac{\partial T}{\partial t}+\mathbf{u}\cdot\nabla T\right)=\nabla\cdot(\kappa\nabla T) \tag{3}$$

where $c_p$ is specific heat and $\kappa$ is thermal conductivity. The solute transport is governed by the balance of species concentration

$$\frac{\partial C}{\partial t}+\mathbf{u}\cdot\nabla C=\nabla\cdot(D\nabla C) \tag{4}$$

where $C$ is the concentration of impurity and $D$ denotes the mass diffusion coefficient. On each segment of the boundary, it is necessary to prescribe appropriate boundary conditions. Details of the computational boundary conditions used in the modeling will be given in section 4.

The change of phase from liquid to solid is described mathematically by the following phase conditions

$$T_l(S,t)=T_s(S,t)=T_m\,, \tag{5}$$

$$\kappa_l\nabla T_l\cdot\hat{\mathbf{n}}-\kappa_s\nabla T_s\cdot\hat{\mathbf{n}}=\rho_s L(\mathbf{u}^s-\mathbf{u}^*)\cdot\hat{\mathbf{n}}\,, \tag{6}$$

$$\rho_l(\mathbf{u}^l-\mathbf{u}^*)\cdot\hat{\mathbf{n}}=\rho_s(\mathbf{u}^s-\mathbf{u}^*)\cdot\hat{\mathbf{n}}\,, \tag{7}$$

$$(\mathbf{u}^l - \mathbf{u}^s) \times \hat{\mathbf{n}} = 0 \tag{8}$$

which need to be satisfied at the solid/liquid interface. Here subscripts and superscripts, $s$ and $l$, refer to the solid & liquid region, respectively; $\mathbf{u}^s$ is the solid pulling velocity; $\mathbf{u}^*$ is the velocity of the interface; $T_m$ is the melting temperature; $\hat{\mathbf{n}}$ is the unit norm of the interface pointing from the liquid to the solid; $L$ is the latent heat of fusion. From a physical point of view, equations (5)-(8) represent thermal equilibrium at the interface; the heat flux balance between the phases which includes latent heat release; the mass flux balance across the interface and the no-slip condition at the liquid side of the interface, respectively.

In order to include the solute (species) transport in the phase change analysis, it is necessary to add two more interface conditions:

$$D_l \nabla C_l \cdot \hat{\mathbf{n}} - D_s \nabla C_s \cdot \hat{\mathbf{n}} = C_s(\mathbf{u}^s - \mathbf{u}^*) \cdot \hat{\mathbf{n}} - C_l(\mathbf{u}^l - \mathbf{u}^*) \cdot \hat{\mathbf{n}}\,, \tag{9}$$

$$C_s = kC_l \tag{10}$$

where $k$ is the partition coefficient. Eqn. (9) describes the mass conservation for solute transport across the interface and eqn. (10) is actually the chemical equilibrium determined by the phase diagram. In this case, the melting temperature depends on solute concentration and condition (5) becomes

$$T_l = T_s = T_m(C) = T_A + mC_l \tag{5'}$$

where $T_A$ is a constant and

$$m = m(C) \equiv \frac{dT_m}{dC} \tag{11}$$

is the rate of change of the melting temperature with respect to $C$. Note that the model summarized in this section assumes a sharp solid/liquid interface; the problem will be solved by the interface tracking approach with deformable grids.

## 4. NUMERICAL SIMULATION

### *4.1 The FEM Model*

In this paper we consider two Bridgman growth configurations. The first is the bottom seeded (vertical) Bridgman growth. In this configuration the hot (melt) zone is on the top and the cold (crystal) zone is at the bottom. The furnace axis is parallel to the gravity vector which is in the vertical direction pointing downwards. For this configuration it is reasonable to assume that the heat, species and flow fields are all axisymmetric. Therefore a simplified axisymmetric model, as depicted in Figure 3, is used to model the vertical Bridgman growth. A 15cm portion of the 90cm-long rod-shaped sample is modeled. The computational boundary conditions imposed for the energy, momentum and species equations are summarized in Figure 4. For the momentum equation, we specify no-slip conditions on the surface between the sample and ampoule wall. For

heat transport, we impose the measured thermal condition on the outer surface of the ampoule. As shown in Fig. 4(b), the thermal profile on the ampoule surface consists of the hot, adiabatic and cold zones. Thermal radiation is not included in the model. Our analysis indicates that for the material and processing temperature range considered, most of the radiation emitted by the heaters gets absorbed by the ampoule and only a small amount of radiation penetrates through the ampoule. And, since we impose the furnace temperature on the ampoule wall, radiation is relatively less important compared to the longitudinal conduction. The concentration boundary conditions are shown in Fig. 4(c).

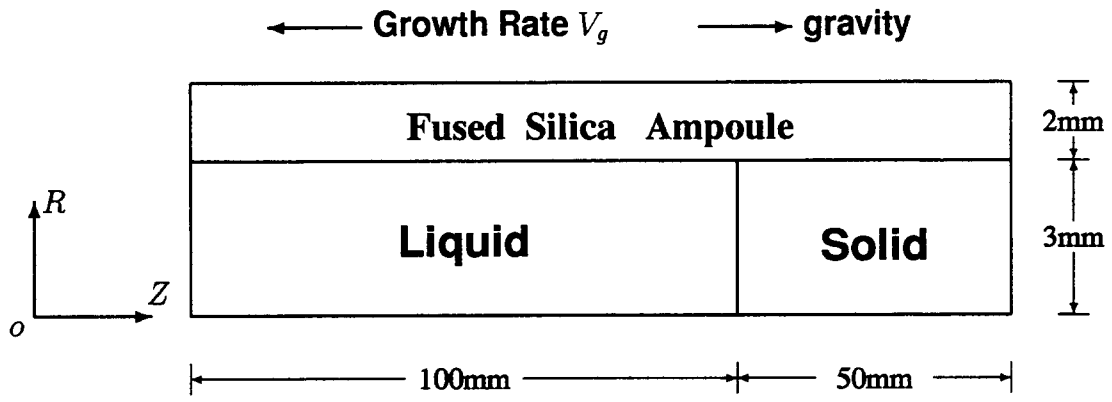


**Figure 3.** Schematic diagram and geometric definitions of a simplified axisymmetric FEM model for the vertical Bridgman growth experiment.

The second configuration is the horizontal Bridgman in which the gravity vector is perpendicular to the furnace axis (i.e. perpendicular to the $z$-axis defined in Fig. 3). In this case, the solutions are assumed to be symmetric about the vertical center plane and an idealized two-dimensional model is used to simulate this center plane. Although this 2-D model is clearly a simplification of the real situation, we hope it can provide at least some qualitative information for this growth configuration. More accurate modeling will rely on the full three-dimensional model which is currently under development.

*4.2 Pseudo-Steady-State Model*

The so-called *pseudo-steady-state model* (PSSM) [25,26] is used to simulate the steady growth of BiSn and SnBi in the vertical and horizontal Bridgman configurations. In PSSM, the translation of the ampoule is modeled by the melt entering at its hot end with a uniform growth velocity $V_g$ and composition $C_0$, and by removing the crystal from the cold end at a speed that conserves the mass of the alloy in the system. Note that as a simplification of the real growth condition, the PSSM neglects the transient effects in the field variables (such as velocity, pressure, temperature and concentration, etc.) caused by the steady decrease of the length of the melt during crystal

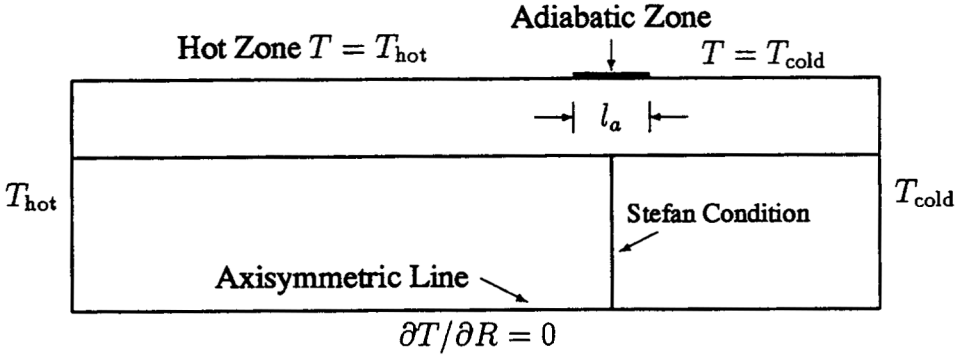


(a) Thermal Boundary Conditions

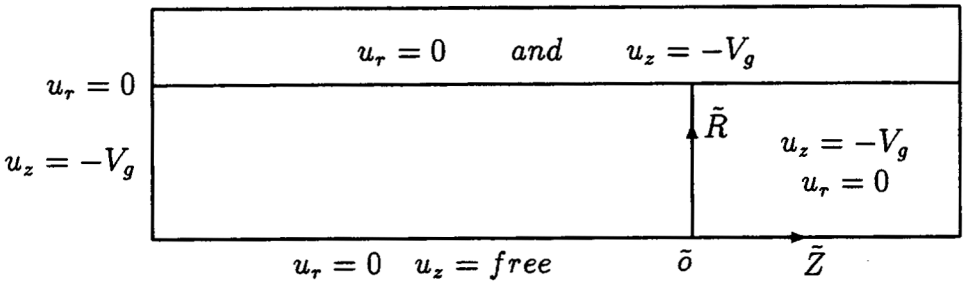


(b) Velocity Boundary Conditions for Pseudo-Steady State Analysis

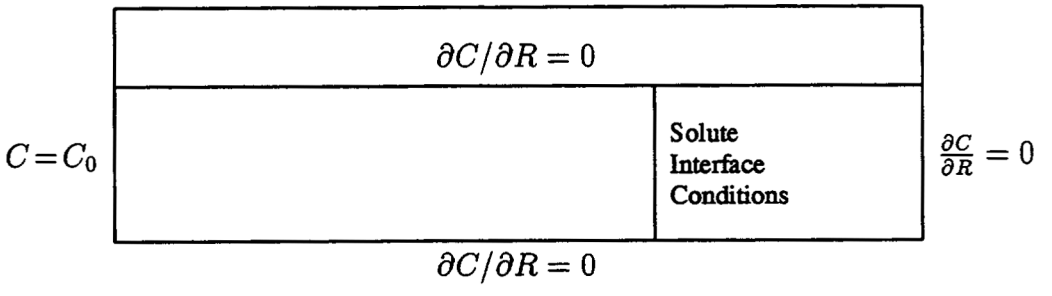


(c) Boundary Conditions for Solute Concentration

**Figure 4.** Computational boundary conditions used for the axisymmetric model.

growth and the displacement of the ampoule in the furnace. It is known that for sufficiently long ampoules the thermal end effects are negligibly small [25]. Another important feature of PSSM is the use of the moving coordinate system by fixing its origin at the center of the moving solid/liquid interface.

*4.3 The Front Tracking Approach*

The most challenging difficulty posed by phase change problems is the moving solid/liquid interface whose position is usually an unknown function of time and space and needs to be determined as a part of the solution. In the literature, various numerical techniques have been proposed to deal with the moving interface for phase change problems [27]. Among them, two main classes of methods can be distinguished, namely the fixed-grid enthalpy methods and the front-tracking methods. The front-tracking technique with a deforming mesh is used in our modeling.

Unlike the enthalpy method, the phase change front tracking method can model the phase change problems with a sharp (single) solid/liquid interface. The front tracking approach used in this work involves a deformable spatial mesh in which nodes located on the interface are allowed to move such that they remain on the moving boundary. For each node on the moving interface, an additional degree of freedom is introduced. This new degree of freedom determines directly the position of the node in space and is an integral part of the representation of the moving interface.

To update the interface position and remesh the interior domains, a method of spines is used. It is a generalization of the method developed by Saito and Scriven [28], in which the moving nodes lie on and the interface movement is guided by the generator lines called *spines*. In particular, the position of the moving node is represented parametrically by

$$\begin{aligned} x_i &= \alpha_x[h_{j+1} + \omega t_i(h_j - h_{j+1})] + \beta_x \\ y_i &= \alpha_y[h_{j+1} + \omega t_i(h_j - h_{j+1})] + \beta_y \\ z_i &= \alpha_z[h_{j+1} + \omega t_i(h_j - h_{j+1})] + \beta_z \end{aligned} \tag{12}$$

where $h_j$ is the interface location parameter for a given spine, $(\alpha_x, \alpha_y, \alpha_z)$ is the direction vector, $(\beta_x, \beta_y, \beta_z)$ is the base point of the spine. The location $(x_i, y_i, z_i)$ of the moving node on the spine is determined from its relative position, $\omega t_i$, to the moving interfaces located at $h_j$ and $h_{j+1}$. Here $h_j$ are the new degree of freedom introduced.

For steady state problems, applying Galerkin's formulation and the standard discretization procedure to the momentum equation (1) results in a nonlinear algebraic system in the following matrix form [29]

$$\mathbf{A(U)U} + \mathbf{K(T,U)} - \mathbf{CP} + \mathbf{BX} = \mathbf{F} \tag{13}$$

where $\mathbf{X}$ is the global vector of the moving interface unknowns, $\mathbf{A(U)}$ accounts for contribution from the convective terms, $\mathbf{K(U)}$ includes the diffusive terms, $\mathbf{C}$ is the matrix discretization of the

divergence, B represents the contribution of the normal stress balance condition at boundary, F is a body force vector.

*4.4 The Segregated Solver*

System (13) along with the energy equation, species equation and other interface and boundary conditions are solved by a segregated solution procedure. In contrast to the traditional fully coupled approach (such as the Newton-type solver), the segregated solution algorithm does not form the global system matrix directly. Instead, it decomposes the global system matrix into smaller sub-matrices each governing the nodal unknowns associated with only one conservation equation. These segregated sub-matrices are then solved in a sequential manner. Since the storage of the individual sub-matrices is considerably less than that needed to store the global system matrix, the storage requirements of the segregated approach are substantially less than those of the fully coupled approach.

*4.5 Special Formulation for Concentration*

A special difficulty in solving mass transfer in phase-change problems is the discontinuity of solute concentration itself across the interface, as indicated by interface condition (10). Furthermore, the melting temperature is no longer a constant; instead it has to be determined by the local solute concentration. However in the standard FEM formulation, both the trial and test function have to be at least $C^0$ continuous, and no jump is allowed for the primitive variables. Therefore, a special treatment is necessary for the species equation.

To eliminate the discontinuity of $C$ at the interface, the following transformation

$$C_s^* = C_s/k \tag{14}$$

is performed for concentration in the solid region. The interface condition (10) is then reduced to

$$C_l = C_s^* \tag{15}$$

and thus $C$ becomes continuous across the phase change interface. It can be proved [30] that the mass flux balance condition (9) can be rewritten in the following form

$$(D_l \nabla C_l - D_s \nabla C_s) \cdot \hat{\mathbf{n}} = h_c C_l \tag{16}$$

where the coefficient

$$h_c = \rho_s(1-k)(\mathbf{u}^s - \mathbf{u}^*) \cdot \hat{\mathbf{n}} + D_s(1-k)\hat{\mathbf{n}} \cdot \nabla C_s^*/C_l \,. \tag{17}$$

The second term in (17) involves spatial gradient of concentration at the solid side. Since the solute diffusivity in solid, i.e. $D_s$, is usually several orders of magnitude smaller than that of the liquid $D_l$, it is reasonable to assume this term is negligible. In our computation, the interface condition (16) is imposed through a species transfer boundary element at the moving interface.

*4.6 Numerical Solution*

The axisymmetric and 2-D FEM models are built with the 4-node bilinear element, in which velocity, temperature and species are approximated by bilinear shape functions. The pressure is approximated as piecewise constant.

In this work, numerical solutions are obtained by using a modified version of the finite element program FIDAP. The details of the FEM formulation in FIDAP are documented in [29]. The nonlinear iteration termination is controlled by a specified tolerance of $10^{-3}$ for the relative error norms of velocity, residual and free surface update.

## 5. PRELIMINARY RESULTS FOR MEPHISTO I

In this section we present our numerical results for the first flight experiment.

*5.1 Two-Step Solution Approach*

In order to simulate the solute segregation, a two-step solution approach was used in our modeling. This two-step approach is based on the assumption that the effect of solute field on the heat transport and fluid motion is negligibly small. Though the validity of this assumption still needs further verification, the main reason for this two-step solution process is the current limitation on the front tracking approach in FIDAP. Due to this limitation, it is impossible to include the conjugate heat transfer, the moving front tracking and the solute segregation all together in one single model.

The two-step solution approach can be briefly described as follows. In step one, we consider a full ampoule model which includes the solid and liquid SnBi sample as well as the glass ampoule wall. A fully coupled heat transport and fluid flow in the liquid SnBi, phase change and the conjugate heat transfer in the ampoule wall are solved simultaneously on the basis of this full ampoule model. Then in step two, we consider the SnBi sample only (without the ampoule wall). On the surface of the SnBi sample, we impose the temperature profile obtained from the first step solution. In this way, the effect of the conjugate heat transfer considered in the full ampoule model is passed to the simplified model in the second step. The solute segregation coupled with heat transport, fluid motion, non-isothermal phase change and mesh deformation are then solved in the second step.

*5.2 Buoyancy-Induced Convection*

To study the effects of gravity on the fluid motion in the melt, we plot the contours of stream function in Fig. 5 for the horizontal growth at various gravity levels ranging from $10^{-6}g$ to $10^{-1}g$. Note that the plots shown in Fig. 5 are based on the total velocity which includes a constant translation velocity and the buoyancy-induced convective velocity. At $10^{-6}g$, the streamlines shown are straight, which indicates that the convective part of the velocity is almost zero. At $10^{-5}g$ the streamlines become slightly curved, but the convective velocity is still very small (about 30% of the growth rate as indicated by the value of $u_{\max}$). This suggests that when gravity $\leq 10^{-5}$g the growth is basically diffusion-controlled and the thermal buoyancy-induced convection is negligible. At the gravity level of $10^{-4}$g, a flow cell has formed in the melt and the flow cell grows bigger

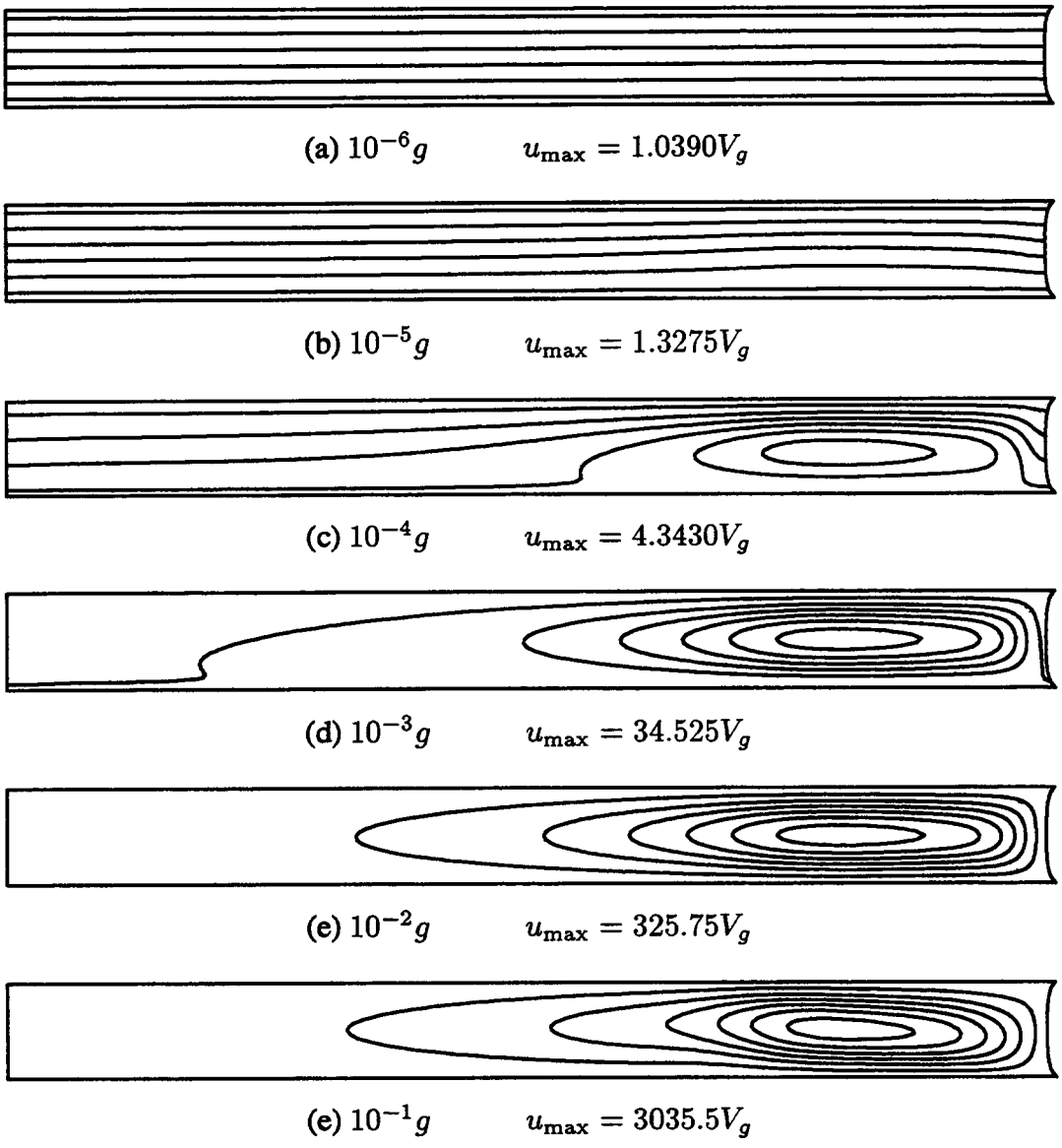


**Figure 5.** Contours of stream functions for the horizontal growth with MEPHISTO I at various gravity levels. Only the liquid part of SnBi sample is plotted and the curved surface on the right is the solid/liquid interface. Here the calculation of stream function is based on the total velocity which includes the growth rate $V_g$ and the buoyancy-induced convective velocity. Namely, $u \equiv u^c + V_g$, where $u^c$ is the convective velocity.

with the increase in gravity. The bigger flow cell corresponds to stronger convection. The shallow cavity flow pattern shown in Fig. 5 agrees well with the flow pattern reported in the literature for the horizontal Bridgman growth [24].

The strength of convection in the melt can be quantified by comparison to the maximum velocity. The effect of gravity on the convection in the melt can be seen more clearly from Fig. 6 in which the total maximum velocity, $U_{\max} = u^c_{\max} + V_g$, versus the magnitude of gravity is plotted for the two growth configurations. The convective strength level marked by the horizontal dashed line in Fig. 6 is important, because at this level the buoyancy-driven convective velocity maximum is the same as the translation velocity (growth rate). It has been shown that radial segregation is often maximum when the convective velocities and the growth rate are similar. Therefore, it can be considered as a critical point for the growth of convective strength in the melt. Let $g_c$ denote the gravity level corresponding to this critical point. For horizontal growth, $g_c \approx 2 \times 10^{-5} g$. When gravity is less than $g_c$, the convection is very weak and grows slowly with increases in $g$. However, when the gravity level exceeds $g_c$, convection grows concomitantly with $g$, and the effects of gravity on the fluid motion in the melt become significant.

For the vertical growth configuration, the buoyancy-induced convection is much weaker than for the horizontal case. It is seen from Fig. 6 that for vertical Bridgman, $g_c \approx 10^{-3} g$, and at the same gravity level convection is about one to two orders of magnitude lower than that of horizontal growth. It is interesting to note that when gravity increases 1000 times from $10^{-3}$g to 1g, $U_{\max}$ also grows about 1000 times. The results presented in Fig. 6 indicate that, above the critical value $g_c$, the effect of gravity on the convection in the melt is very significant.

*5.3 Solute Distribution in the Melt*

For a given bulk alloy, the solute concentration at the interface is affected by the removal rate of excess solute atoms rejected at the moving interface. Under ideal conditions (no convection), the rejected solute is transported by diffusion only. In reality, however, the transport of excess solute atoms to and from the interface is greatly affected by additional factors such as the buoyancy force caused by density gradient. In this work, the density variation with temperature is modeled by the Boussinesq approximation given in eqn. (1). For SnBi, a positive change of $\Delta T$ will reduce the density in the buoyancy term in the momentum equation. The segregation coefficient $k < 1$ and $\rho_{\text{solute}} > \rho_{\text{solvent}}$ imply that heaver solute is rejected at the interface. Consequently, the double-diffusive convection is solutally stable in a classical vertical growth system.

For MEPHISTO 1, the initial concentration of Bi in the SnBi alloy was $C_0 = 0.5$ at.%. As predicted by the convective strength, the growth is diffusion-dominated at the microgravity level of $10^{-6} g$. To verify the numerical results, we compare the simulated solute distribution on the centerline of the 2-D horizontal growth model against the available 1-D analytical solution. It is seen from Fig. 7 that the modeled solute boundary layer at $10^{-6} g$ is indeed very close to the diffusion-controlled solution.

In order to describe quantitatively the transition from diffusion-controlled growth (without

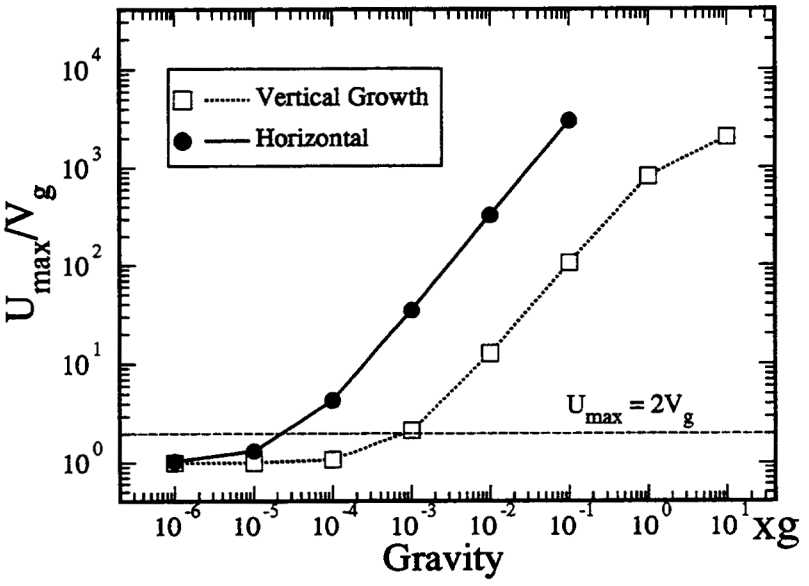


**Figure 6.** Effects of gravity on the strength of convection in the melt measured by the maximum total velocity, $U_{max}$, which includes the growth rate $V_g$ and the thermal buoyancy-driven convective velocity.

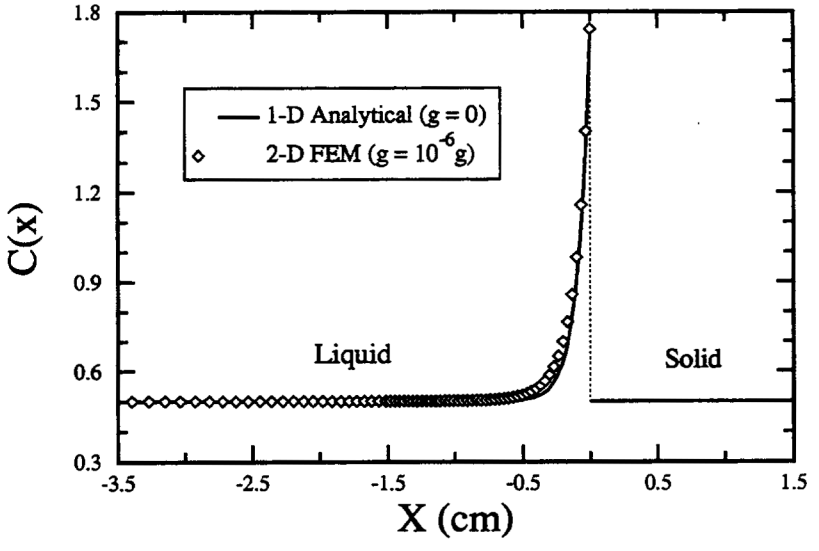


**Figure 7.** Comparison of the simulated axial solute distribution on the centerline of the SnBi sample with the 1-D diffusion-controlled growth solution. The FEM result is based on the 2-D model for the horizontal configuration. In order to display the thin boundary layer, only a portion of the entire centerline is shown.

bulk convection) to growth with intensive laminar convective mixing, we compute two important segregation parameters. The first is the *effective segregation coefficient* $k_{\text{eff}}$ defined as [26]

$$k_{\text{eff}} \equiv k < C >_I \; / \; \ll C \gg \tag{18}$$

where $< C >_I$ is the lateral average of solute concentration over the solid/liquid interface and $\ll C \gg$ is the volumetric average of solute concentration in the melt. The second is the percentage radial segregation $\Delta C$ defined as

$$\Delta C \equiv |\delta C|_{\max} / C_0 \tag{19}$$

or

$$\Delta C \equiv |C_{\text{top}} - C_{\text{bottom}}| / C_0 \; . \tag{20}$$

Here $|\delta C|_{\max}$ is the maximum difference in liquid concentration at the interface. For directional solidification, the diffusion-controlled growth with a planar interface leads to uniform radial solute distribution, thus we may have $\Delta C \approx 0$. However, if the s/l interface is not flat, for example, due to radial temperature gradients, significant radial solute gradients may develop even under diffusion-controlled conditions. If the melt is sufficiently long that the diffusion layer near the interface occupies only a small fraction of the total length, $k_{\text{eff}}$ approaches unity when there is no convective flow in the melt other than the unidirectional growth velocity $V_g$. The other limit of $k_{\text{eff}}$ represents the steady-state well-mixed growth in which the intense convection leads to a complete mixing in the melt. In this case the value of $k_{\text{eff}}$ approaches $k$.

The computed $k_{\text{eff}}$ and $\Delta C$ for both the vertical and horizontal growth are plotted as a function of gravity levels in Figs. 8 and 9, respectively. For the vertical growth case, the values of $k_{\text{eff}}$ are very close to one when gravity is less than $10^{-2}g$ as shown in Fig. 8(a). The value of $k_{\text{eff}}$ starts to decrease rapidly at $10^{-2}g$ and does approach $k$ with increasing gravity levels. The corresponding radial segregation presented in Fig. 9(a) shows that there is a radial solute gradient at the interface even in the diffusion dominated growth range. The radial segregation reaches a maximum at about $10^{-2}g$ and then decreases with the increase of gravity. The radial segregation in the liquid is caused by the nonplanar shape of the interface, and since we feel improvements are still possible in our interface shape results, we will be examining segregation in more detail in a later paper. For the horizontal configuration, the value of $k_{\text{eff}}$ starts to decrease dramatically at a much lower gravity level of $10^{-4}g$, because of the much stronger convection. It is seen from Fig. 8(b) that $k_{\text{eff}}$ is very close to $k$ at $10^{-1}g$ which indicates that a well-mixed state has been achieved at this gravity level. Note that although the values of the radial segregation computed by eqns. (19) and (20) are different, the predicted maximum $\Delta C$ occurs at the same gravity level of $10^{-4}g$ for horizontal growth as shown in Fig. 9(b). The plots of $k_{\text{eff}}$ and $\Delta C$ vs. the magnitude of gravity presented here agree very well with the schematic curves given by Kim, Adornato and Brown in [26].

By considering the worst orientation of gravity vector during the space experiment (namely the horizontal configuration), the results presented in Figs. 8 and 9 suggest that the growth is basically

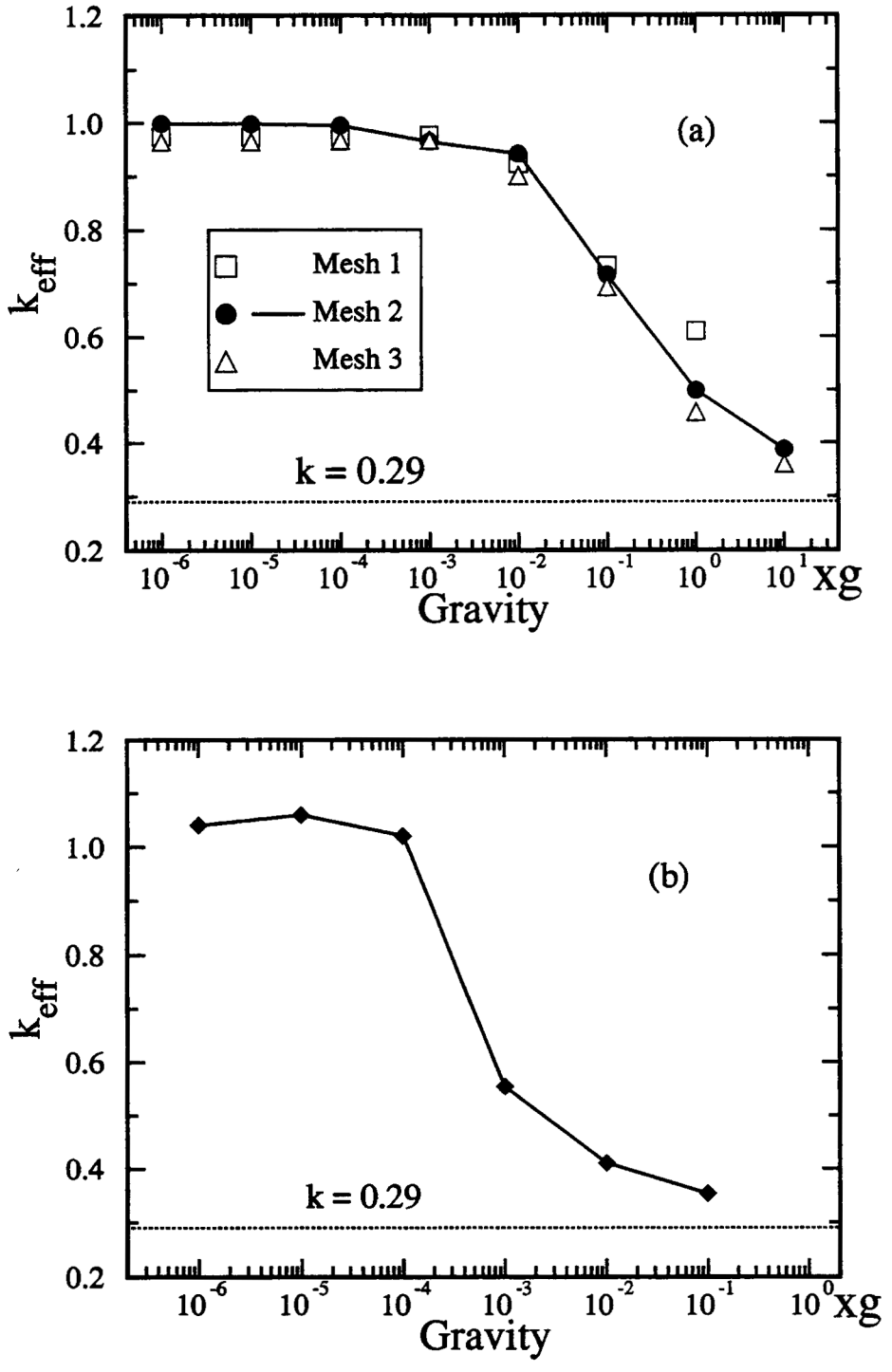


**Figure 8.** Effects of gravity on the axial solute segregation measured in terms of the effective segregation coefficient, $k_{\text{eff}}$. (a) For the vertical growth; (b) for the horizontal configuration.

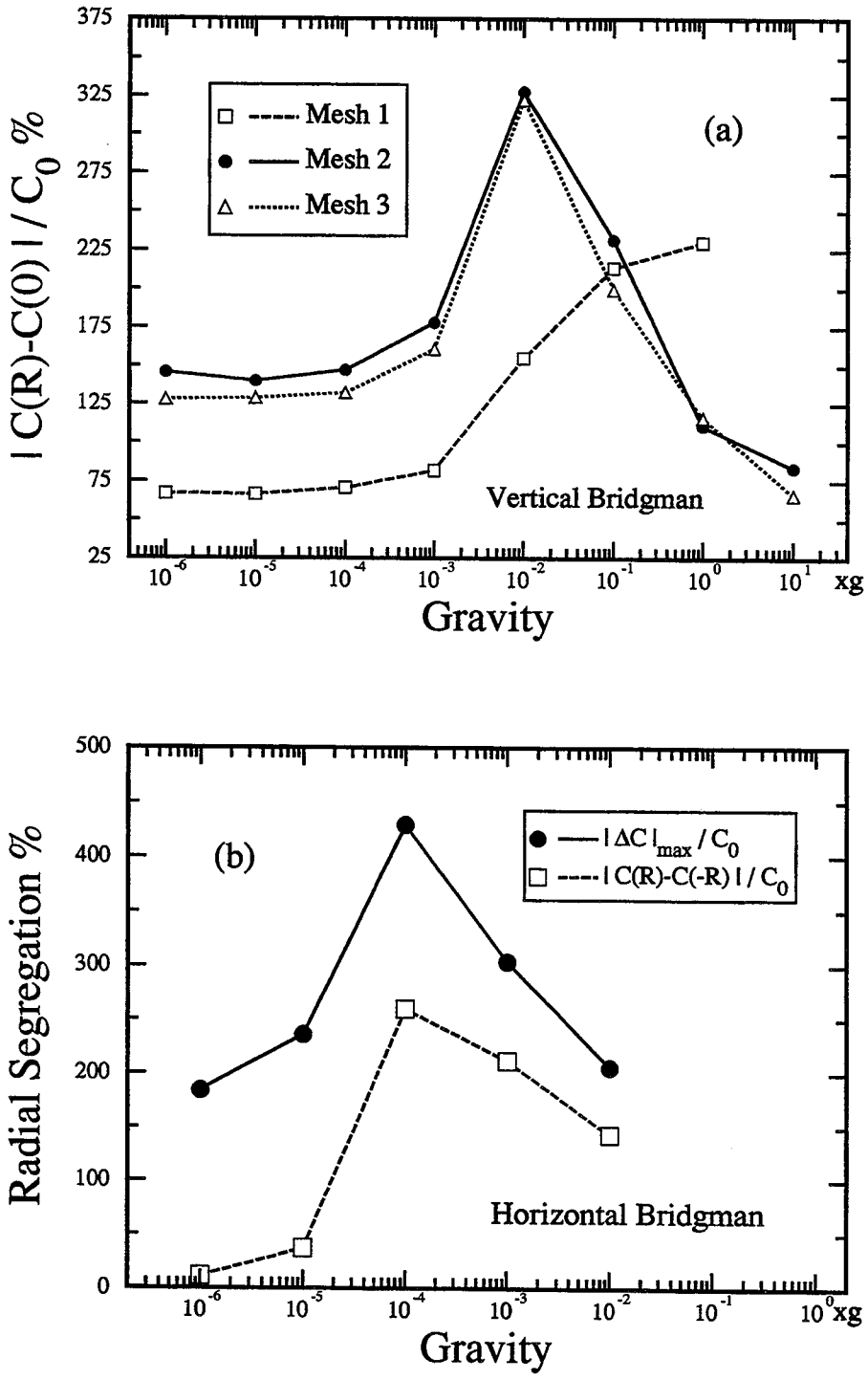


**Figure 9.** Effects of gravity on the radial solute segregation. Note that the values of $\Delta C$ were calculated from the liquid side of the interface. (a) For the vertical growth; (b) for the horizontal configuration, where $C(R)$ is the liquid composition at the top of the ampoule and $C(-R)$ is at the bottom.

diffusion-controlled when the magnitude of gravity is less than $10^{-5}g$. Therefore our numerical observation supports the diffusion-controlled growth assumption used by the French team [13,16]. Another interesting point is the gravity level at which the radial segregation reaches its maximum. For both growth configurations, the maximum $\Delta C$ occurs at the approximate ending point of the gravity range over which $k_{\text{eff}}$ indicates diffusion-controlled growth. For example, for the horizontal growth the ending point of the gravity range for $k_{\text{eff}} \approx 1$ is $10^{-4}g$, that is exactly the same gravity level at which $\Delta C$ has its maximum, as one can see from Fig. 8(b) and Fig. 9(b). Actually this gravity level corresponds to a weak convection in the melt with an incomplete mixing of solute. This in turn leads the concentration field adjacent to the interface highly distorted and the amount of radial segregation reaches its maximum, though the axial segregation (measured by $k_{\text{eff}}$) indicates diffusion-controlled growth.

*5.4 Convergence of Numerical Solutions*

In order to check the convergence and accuracy of the numerical solutions, a set of three meshes were used in the modeling for the vertical growth case. The three meshes are referred to as mesh 1 to 3 in Fig. 8(a) and Fig. 9(a). Mesh 1 is the coarsest with a total of 820 bilinear elements and 913 nodes. Mesh 2 is the intermediate with a total of 1344 elements and 1469 nodes. Mesh 3 is the finest with about 3000 elements.

For velocity, the numerical solutions from the three meshes are all very close. For example the difference between the maximum velocities predicted by mesh 1 and mesh 3 is less than 1%, which suggests that even mesh 1 can provide a very good solution for velocity. Our analysis shows that the most difficult variable for numerical convergence is the solute concentration, perhaps due to the very thin solute boundary layer near the interface. For the effective segregation coefficient, the results presented in Fig. 8(a) show that when gravity is less than $10^{-1}g$ the values of $k_{\text{eff}}$ computed from the three meshes are very close. But the error of the mesh 1 becomes unacceptable at 1g. For the calculation of the radial segregation, mesh 1 fails completely as can be seen in Fig. 9(a). This suggests that a coarse mesh is not capable of resolving the thin solute boundary layer. In all the cases, the differences between the solutions obtained from meshes 2 and 3 are very small. Our experience also indicates that grading towards the interface (i.e. gradually reducing element size towards interface) helps improve the solution accuracy for solute concentration.

## 6. PRELIMINARY RESULTS FOR MEPHISTO II

For MEPHISTO 2, seven gravity levels were considered: $10^{-6}$g, $10^{-5}$g, $10^{-4}$g, $10^{-3}$g, $10^{-2}$g, $10^{-1}$g and 1g. The $10^{-6}$g to $10^{-3}$g cases simulate the range of accelerations expected during space processing and the 1g case simulates ground based experiments.

Figs. 10(a), 10(b) and 10(c) show the velocity vectors for three gravity levels for the vertical configuration. It is seen that the flow cell forms at a g-level of $10^{-5}$g and builds up as gravity increases. At a gravity level of $10^{-3}$g, the flow velocities become comparable to the growth velocity.

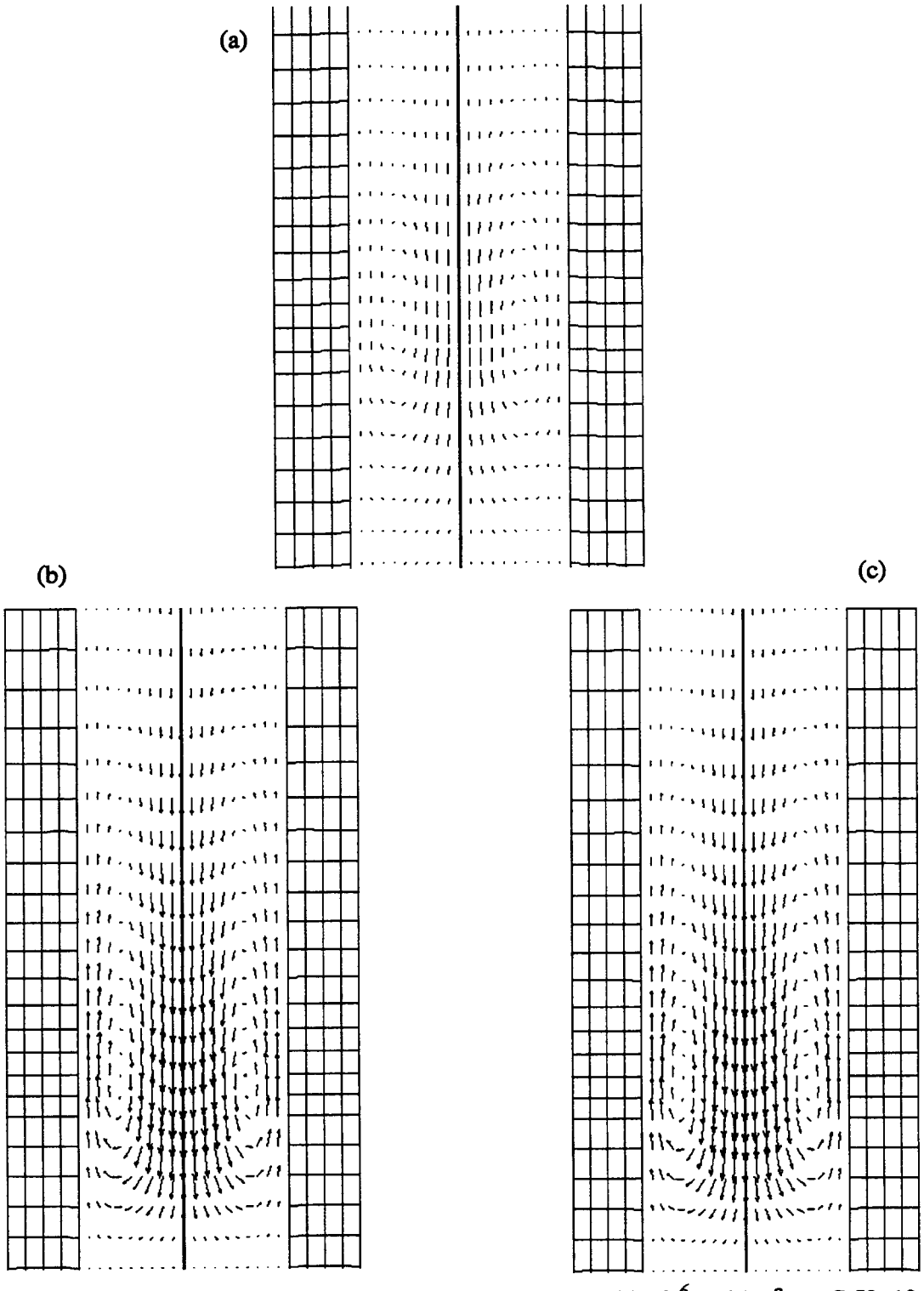


**Figure 10.** BiSn, vertical configuration: convective cells at (a) $10^{-6}$g with $u^c_{max}$=7.53x$10^{-7}$ cm/sec, (b) $10^{-3}$g with $u^c_{max}$=7.72x$10^{-4}$cm/sec, and (c) 1g with $u^c_{max}$=2.59x$10^{-1}$ cm/sec.

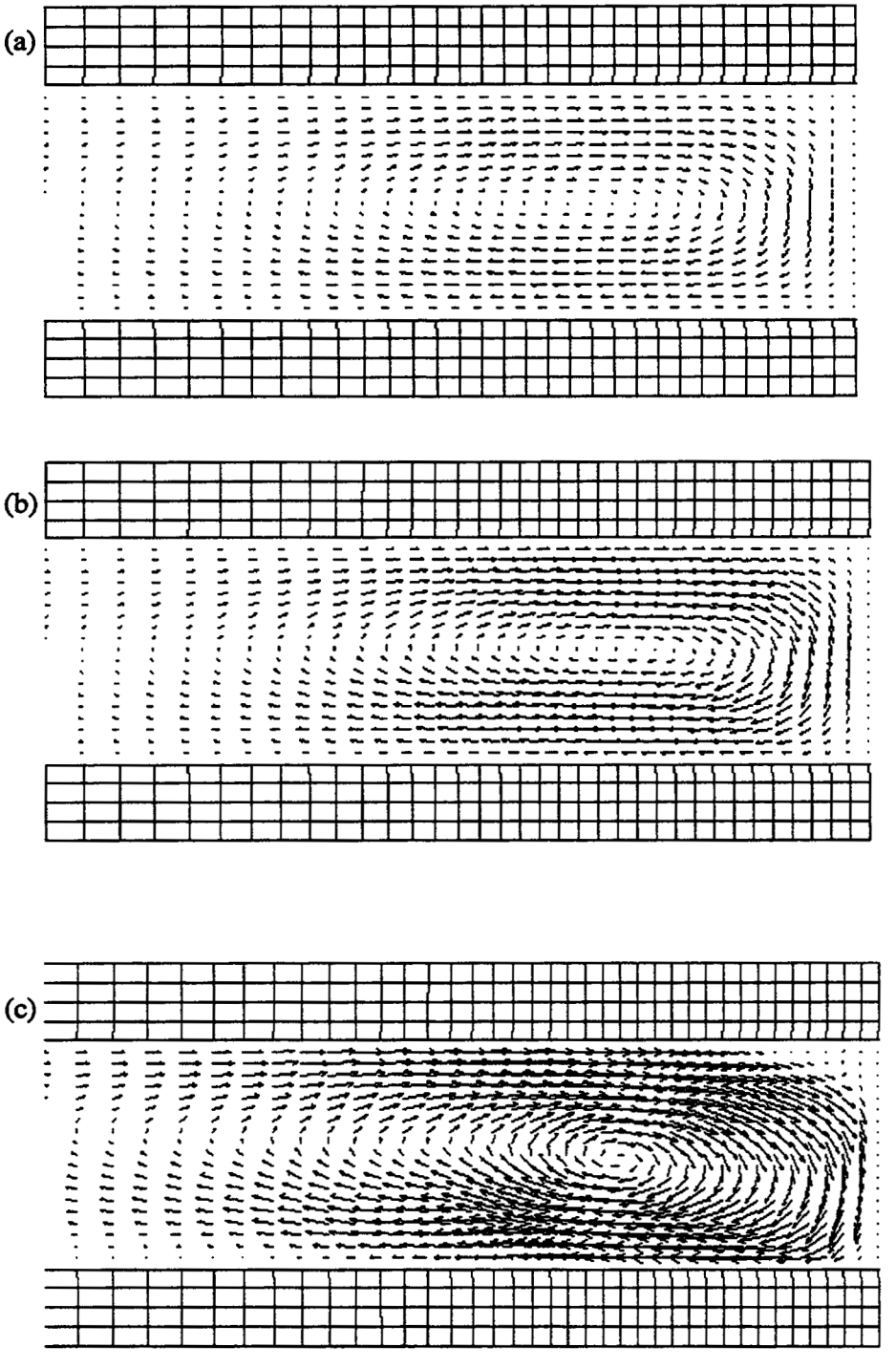


**Figure 11.** BiSn, Horizontal configuration: Convective cells for (a) $10^{-6}$g with $u^c_{max}$=2.02x$10^{-5}$ cm/sec, (b) $10^{-3}$g with $u^c_{max}$=2.04x$10^{-2}$ cm/sec, (c) 1g with $u^c_{max}$=3.72 .

A very strong convective cell is seen for the 1g case. Figs. 11(a), 11(b) and 11(c) show the velocity vectors for three gravity levels for the horizontal configuration. It is seen that the velocities are greater and stronger convective cells are formed for this configuration.

To clearly correlate the effect of gravity on the flow velocities, the ratio of the maximum velocity to the growth velocity $V_g$ was plotted against each g-level in Fig. 12. This plot shows that the log of the velocity ratio is nearly linear with the log of the gravity. This means that $u^c_{max}$ grows with the same order of magnitude as the gravity level. Fig. 12 also compares the growth of $u^c_{max}$ for the horizontal configuration. It is interesting to see that the slope is nearly the same for this case, showing that the flow velocities are consistently an order of magnitude higher for the horizontal configuration.

It has been shown here and by others[2] that the greatest amount of radial segregation occurs when convective velocities near the interface are close to the solidification rate ($u^c_{max}/V_g$ approximately = 1). Fig. 12 shows that for the vertical case, convective levels are expected to be most damaging to the radial homogeneity at about $10^{-3}$g, because convective velocities are about the same as the growth velocity.

For the horizontal case however, concern for radial homogeneity is justified at about $3x10^{-5}$ g. The steady state background g-levels on the Space Shuttle are generally accepted to be less than $10^{-5}$g, thus steady g-levels imply diffusion controlled growth for MEPHISTO-2 since convective levels are expected to be significantly less than the growth velocity.

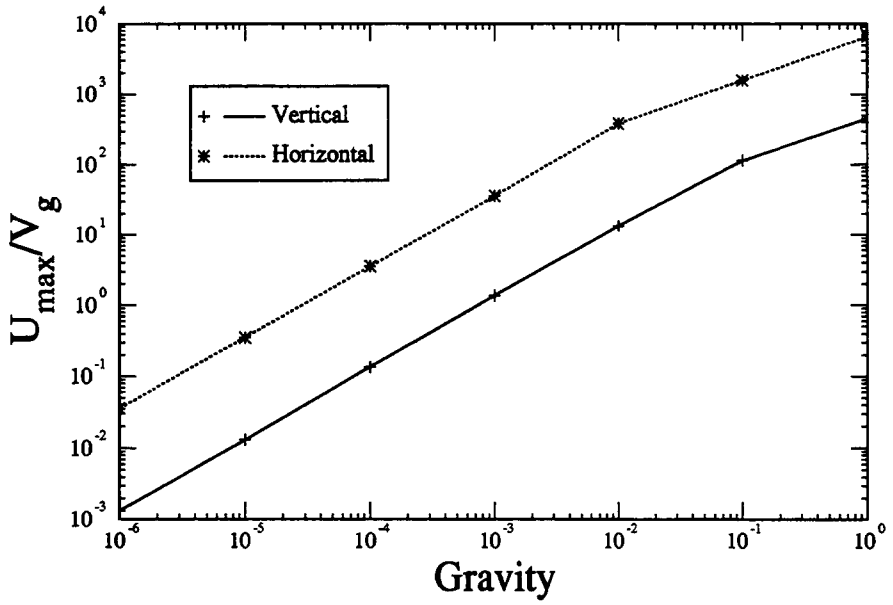


**Figure 12.** A log-log plot of $u^c_{max}/V_g$ vs. g-levels showing the effect of gravity on convective maximum velocities for MEPHISTO 2.

Residual gravity transients caused by thruster firings and other disturbances are often in the range of $10^{-4}$g and greater for short periods; the response of solidification processes to non-steady gravity is presently under investigation and will be dealt with in a later paper. However, results from the first flight of MEPHISTO show experimental indications of convection during, for example, crew exercise, when the magnitude of the transient acceleration is in the range of $5x10^{-4}$g.

The sample temperature in the hot and cold zones and the profile through the adiabatic zone, which was calculated as part of the solution, are shown in Fig 13. The temperature contours for two gravity levels for the horizontal configuration are shown in Fig 14. It is clear that the contours become distorted by the flow field, with warmer liquid traveling along the top wall and cooler liquid returning along the bottom. For the vertical configuration, the distortion is much less because the velocities are lower. However, since at 1-g in the horizontal orientation, the interface is expected to be curved (with the solid concave, or female)[5] further modeling of the interface shape is presently underway.

During the first flight of MEPHISTO, under some conditions, convection in the melt was indicated by fluctuations in the interface temperature (as measured using the Seebeck technique). By nondimensionalizing these conditions we can project convective conditions to MEPHISTO 2, and in combination with the numerical modeling results, estimate the relative influence of convection and diffusion during MEPHISTO. The Prandtl number, $Pr = \frac{\nu}{\alpha}$, compares the rate of diffusion of momentum and heat where $\nu$ is the dynamic viscosity and $\alpha$ is the thermal diffusivity. The Schmidt number, $Sc = \frac{\nu}{D}$, similarly compares diffusivities of momentum and species where

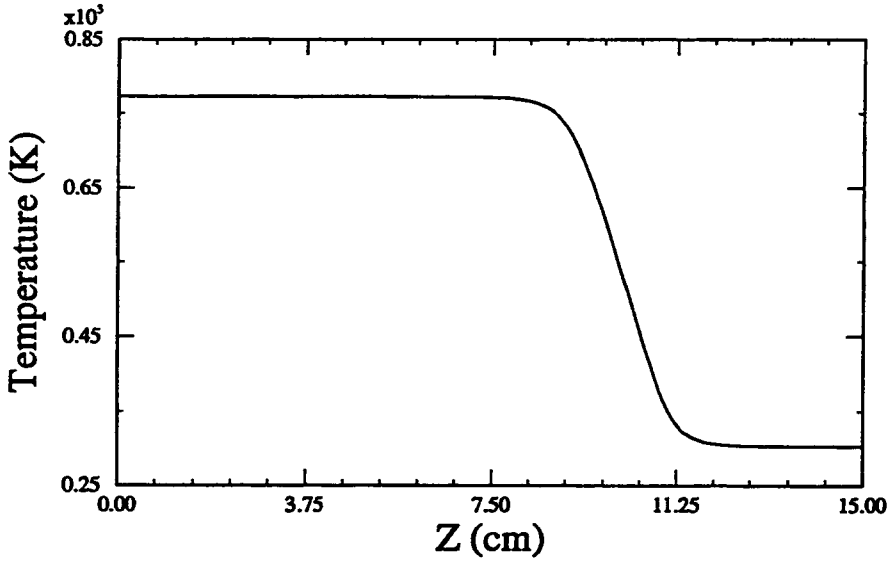


**Figure 13.** BiSn, calculated temperature profile at the center-line of the sample (R=0) for the vertical configuration based on the 2D axisymmetric model.

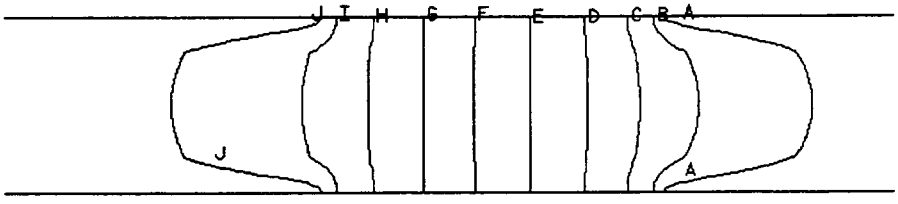


(a) GRAVITY = $10^{-6}$g

Key:

A: 326.5 K

J: 749.5 K

ΔT = 47 K

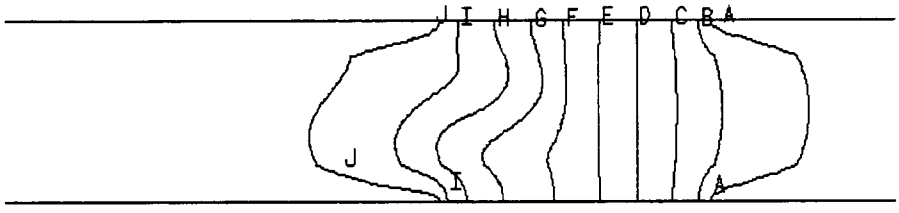


(b) GRAVITY = 1g

**Figure 14.** MEPHISTO 2 temperature contour plots for (a) $10^{-6}$g and (b) 1g in the horizontal configuration. The temperature difference between isotherms is 47K.

$D$ is the species diffusivity. The thermal Grashof number is given by:

$$Gr_T = \frac{g\beta_T \Delta T L^3}{\nu^2}$$

where $\beta_T$ is the coefficient of thermal expansion, $\Delta T = T_h - T_m$ is the temperature difference between the hot zone, $T_h$, and the alloy melting temperature, $T_m$. The distance over which $\Delta T$ is active is L, the characteristic length of the system, i.e., the longitudinal distance between $T_h$ and $T_m$ (L≈3.7cm for MEPHISTO I, L≈2 cm for MEPHISTO 2). The solutal Grashof number is given by,

$$Gr_s = \frac{g\beta_c \Delta C \delta^3}{\nu^2}$$

where $\beta_c$ is the solutal expansivity, the characteristic length, δ, is the boundary-layer thickness and $\Delta C$ is the concentration difference between the far field liquid and the liquid at the interface. The solutal Peclet number is given by $Pe = u^c_{max}\delta/D$, where $u^c_{max}$ is the maximum convective flow velocity in the melt. Table 1 shows the dimensionless groups for MEPHISTO 1 and 2. Prandtl and Schmidt numbers were evaluated at 20 K above $T_m$.

The thermal Grashof numbers for the MEPHISTO experiments are of the same order, thus convective mixing is expected during crew exercise (at g levels above about 300 μg) and during such activities as major truster firings (at 2500μg) as was observed during MEPHISTO 1.

Amounts of convection insufficient to cause disturbances detected by Seebeck interface temperature measurements may still influence the solidification process significantly. For example, rather slow flow velocities have been shown to be most detrimental to radial homogeneity (Brown (1988), Yao and de Groh (1994)). The solutal Peclet numbers shown in Table 1 indicate that convective and diffusive transport are of the same order when gravity is in the 10 to 100 μg range. This indicates that for MEPHISTO 1 and 2 diffusion-dominated growth was likely during sleep periods (at g levels less than about 5μg). This is consistent with Fig. 9 results, which show the radial solutal gradient in the liquid to be relatively small at g levels below $10^{-5}$g.

## 7. CONCLUSIONS

The goal of this work was to, using numerical techniques, quantify buoyancy-driven convection during Bridgman solidification and to determine the effect of gravity on convective velocities in the vertical and horizontal configurations for two recent NASA space experiment projects, MEPHISTO 1 and 2. For MEPHISTO 1, the solute field was included in our analysis, however, for MEPHISTO 2, solute was omitted.

Numerical simulation indicates that the buoyancy-induced convection in the melt intensifies quite rapidly as gravity increases. At equivalent gravity, flow velocities occurring during horizontal conditions were about 15 times greater than those during vertical growth for both MEPHISTO 1 and 2. By considering the worst orientation of gravity vector during the space experiment (namely the horizontal configuration), our results suggest that the growth is basically diffusion-controlled at $g$-levels below $10^{-5}g$ for both MEPHISTO 1 and 2. Therefore our numerical observation supports the diffusion-controlled growth assumption [13] and the assumption that under quasi-diffusive conditions residual convection does not perturb the concentration field significantly at low $g$-levels [16] used in the analysis by the French team.

## ACKNOWLEDGMENTS

This work was supported by NASA's Micro-gravity Science and Application Program (Grant # NAG 3-1096 and NCC 3-208). The authors wish to thank R. Abbaschian, A. Gokhale, J.J. Favier and the rest of the MEPHISTO team for their helpful guidance. We also would like to thank Natarajan Ramanan at Fluid Dynamics International for technical support and very helpful comments on using the free surface solution approach in FIDAP. The authors are grateful to Thomas Glasgow, Mohammad Kassemi and Emily Nelson for their review and valuable comments.

## REFERENCES


[1] M.C. Flemings, *Solidification Processing*, McGraw-Hill, p. 42 (1974).

[2] M.A. Brown, Theory of transport processes in single crystal growth from the melt, *AIChE J*, Vol. 34 (1988), pp. 881-911.

[3] M. Yao and H.C. de Groh III, Three-Dimensional Finite Element Method Simulation of Bridgman Crystal Growth and Comparison with Experiments, *Num. Heat Transf., Part A*, Vol. 24 (1993), pp. 393-412.

[4] D. Gadonniex, A. Gokhale, and R. Abbaschian, Morphological Stability of Faceted Solid/Liquid Interfaces in Dilute Bi-Sn Alloys, 32nd Aerospace Sci. Meeting, Jan. 1994, AIAA 94-0791.

[5] H.C. de Groh III and T. Lindstrom, Interface Shape and Convection during Solidification and Melting of Succinonitrile, NASA TM 106487 (1994).

[6] R. Abbachian, A.B. Gokhale, J.J. Favier and S.R. Coriell, In-Situ Monitoring of Crystal Growth Using MEPHISTO, NASA Science Requirements Document, October, 1992.

[7] E. Nelson, An Examination of Anticipated g-jitter on Space Station and its Effects on Materials Processes, NASA TM 103775, May 1991.

[8] M.J.B. Rogers, C.R. Baugher, R.C. Blanchard, R. DeLombard, W.W. Durgin, D.H. Matthiesen, W. Neupert, and P. Roussel, Low Gravity Environment On-board Columbia During STS-40, 31st Aerospace Sci. Meeting, AIAA 93-0833, 1993.

[9] R.C. Blanchard, J.Y. Nicholson, and J.R. Ritter, Preliminary OARE Absolute Acceleration Measurements on STS-50, NASA TM 107724, Feb. 1993.

[10] G.L. Martin, C.R. Baugher, F. Henderson, STS-52 Mission Acceleration Measurements Summary - Sensor Report, Acceleration Characterization and Analysis Project, Space Sci. Lab., NASA Marshall Space Flight Center, Sept. 1993.

[11] R.J. Schaefer and S.R. Coriell, Convection-induced distortion of a solid-liquid interface, *Metall. Trans. A*, Vol. 15A, 1994, pp. 2109-2115.

[12] H.C. de Groh III and E.S. Nelson, On Residual Acceleration During Space Experiments, in *Heat Transfer in Microgravity Systems*, edited by S.S. Sadhal and A. Gopinath, HTD-Vol. 290, ASME 1994, pp. 23-33.

[13] J.J. Favier, J.P. Garandet, A. Rouzaud and D. Camel, Mass Transport Phenomena during solidification in Microgravity; Preliminary Results of the First Mephisto Flight Experiment, *J. Crystal Growth*, Vol. 140 (1994) pp. 237-243.

[14] J.P. Garandet, J.J. Favier and D. Camel, Solute Boundary Layer Concept and Scaling Analysis: Two Keys to Segregation Phenomena in Melt Crystal Growth, *J. Crystal Growth*, Vol. 130 (1993) 113-122.

[15] S.R. Coriell, R.F. Boisvert, G.B. McFadden, L.N. Brush and J.J. Favier, Morphological Stability of A Binary Alloy During Directional Solidification: Initial Transient, *J. Crystal Growth*, Vol. 140 (1994) pp. 139-147.

[16] J.P. Garandet, Convection Related Radial Segregation in A Idealized Horizontal Bridgman Configuration; The Quasi Diffusive Regime Limit, *J. Crystal Growth*, Vol. 125 (1992) pp. 112-120.

[17] R.J. Schaefer and S.R. Coriell, Convection-Induced Distortion of A Solid-Liquid Interface, *Metall. Trans. A*, Vol. 15A (1994) pp. 2109-2115.

[18] S.R. Coriell and G.B. McFadden, Instability During Directional Solidification: Gravitational Effects, in *Low-Gravity Fluid Dynamics and Transport Phenomena*, ed. Koster and Sani, Vol. 130, AIAA (1990) pp. 369-384.

[19] D. Thevenard, A. Rouzaud, J. Comera and J.J. Favier, Influence of Convective Thermal Oscillations on A Solidification Interface in Bridgman Growth, *J. Crystal Growth*, Vol 108 (1991) pp. 572-582.

[20] M.D. Dupouy, D. Camel and J.J. Favier, Natural Convection in Directional Dendritic Solidification of Metallic Alloys-I: Macroscopic Effects, *Acta Metall.* Vol 37 (1989) pp. 1143-1157.

[21] M. Hennenberg, A. Rouzaud, D. Camel and J.J. Favier, Morphological and Thermosolutal Instabilities inside A Deformable Solute Boundary Layer during Unidirectional Solidification, *J. Crystal Growth*, Vol. 85 (1987) pp. 49-58.

[22] J.J. Favier and D. Camel, Analytical and Experimental Study of Transport Processes during Directional Solidification and Crystal Growth, *J. Crystal Growth*, Vol. 79 (1986) pp. 50-64.

[23] A. Rouzaud, D. Camel and J.J. Favier, A Comparative Study of Thermal and Thermosolutal Convective Effects in Vertical Bridgman Crystal Growth, *J. Crystal Growth*, Vol. 73 (1985) pp. 149-166.

[24] W.A. Arnold, D.A. Jacqmin, R.L. Gaug and A. Chait, Three-Dimensional Flow Transport Modes in Directional Solidification during Space Processing, *J. Spacecraft and Rockets*, Vol. 28 (1991) pp. 238-234.

[25] P.M. Adornato and R. Brown, Convection and Segregation in Directional Solidification of Dilute and Non-Dilute Binary Alloys: Effects of Ampoule and Furnace Design, *J. Crystal Growth*, Vol. 80 (1987) pp. 155-190.

[26] D.H. Kim, P.M. Adornato and R. Brown, Effect of Vertical Magnetic Field on Convection and Segregation in Vertical Bridgman Crystal Growth, *J. Crystal Growth*, Vol. 89 (1988) pp. 339-356.

[27] J. Crank, *Free and Moving Boundary Problems*, Clarendon Press, Oxford, 1984.

[28] H. Saito and L.E. Scriven, Study of Coating Flow by the Finite Element Method, *J. comp. Phys.*, Vol. 42, 53 (1981).

[29] M. Engleman, *FIDAP Theoretical Manual (version 7)*, Fluid Dynamics International, Inc., 500 Davis St. Suite 600, Evanston, IL 60201, 1993.

[30] N. Ramanan, A Note on Derivation of Transfer Coefficient for Species Transfer Boundary Element, (private communication) 1993.

[31] S.Z. Beer, editor, *Liquid Metals*, 1972, Marcel Dekker Inc., New York, p. 186.

[32] H.E. Boyer and T.L. Gall, editors, *Metals Handbook*, Desk Edition, 1985, ASM, Metals Park, Ohio, p. 144.

[33] Y.S. Touloukian et al., editors, *Thermophysical Properties of Matter*, the TPRC Data Series Volumes 1,2,4,5, and 11, 1970, Purdue Research Foundation, IFI/Plenum.

[34] Niwa et al., *J of M*, Jan. 1957, p. 96.

Table 1Physical Property Data for amorphous $SiO_2$ ampoule, Bi, and Sn.[31-34]

| Property | Ampoule | Bi solid | Bi liquid | Sn solid | Sn liquid |
|---|---|---|---|---|---|
| Density, ρ, g/cc | 2.20 | 9.80 | 10.07 | 7.30 | 7.00 |
| Melting point, $T_m$, °C | | 271.3 | | 231.912 | |
| Heat of fusion, ΔH, cal/g | | 12.5 | | 14.5 | |
| Thermal expansion coef., β, $K^{-1}$ | | | $-125x10^{-6}$ | | $-88x10^{-6}$ |
| Diffusivity of Sn in liquid Bi: $D_{Sn\ in\ Bi} = 5.2x10^{-4}(exp(-3.2kcal\text{-}mol^{-1}/RT)\ cm^2/s$ | | | | | |
| Diffusivity of Bi in liquid Sn: $D_{Bi\ in\ Sn} = 3.355x10^{-4}(exp(-2.98kcal\text{-}mol^{-1}/RT)\ cm^2/s$ | | | | | |
| Viscosity, μ, cP: Liquid Bi: $\mu = 0.4458cP\ exp[1.541\ kcal\text{-}mol^{-1}/RT]$ | | | | | |
| Liquid Sn: $\mu = 0.5382cP\ exp[1.3\ kcal\text{-}mol^{-1}/RT]$ | | | | | |
| Partition coefficient for Bi rich alloy with Sn, $k = 3.5x10^{-3}$ at%/at% | | | | | |
| Partition coefficient for Si rich alloy with Bi, k = 0.29 at%/at% | | | | | |
| Thermal conductivity, k, W/cm-K: | | | | | |
| at 300 K | | 0.0786 | | 0.666 | |
| 400 K | | 0.0704 | | 0.622 | |
| 423 K | 0.0189 | | | | |
| 473 K | 0.0192 | | | | |
| 500 K | | 0.0663 | | | |
| 505 K | | | | 0.595 | |
| 506 K | | | | | 0.303 |
| 544 K | | 0.065 | | | |
| 545 K | | | 0.124 | | |
| 573 K | 0.0201 | | | | |
| 600 K | | | 0.131 | | 0.323 |
| 673 K | 0.0213 | | | | |
| 700 K | | | 0.141 | | 0.343 |
| 773 K | 0.0222 | | | | |
| 800 K | | | 0.15 | | 0.364 |
| 873 K | 0.023 | | | | |
| 900 K | | | 0.159 | | 0.384 |
| 973 K | 0.0239 | | | | |
| Specific heat, $C_p$, cal/g-K: | | | | | |
| at 300 K | 0.17 | 0.0295 | | 0.055 | |
| 400 K | 0.21 | 0.031 | | 0.058 | |
| 500 K | 0.235 | 0.033 | | 0.063 | |
| 506 K | | | | | 0.064 |
| 520 K | | 0.034 | | | |
| 534 K | | 0.043 | | | |
| 538 K | | 0.0567 | | | |
| 545 K | | | 0.0346 | | |
| 600 K | 0.25 | | 0.0336 | | 0.0586 |
| 700 K | 0.26 | | 0.0326 | | 0.0568 |
| 800 K | 0.27 | | 0.0321 | | 0.055 |
| 900 K | 0.28 | | | | |

Table 2 Approximate furnace hot and cold zone temperature ranges in °C, adiabatic zone lengths in mm, angle off vertical between g and the ampoule axis in degrees - for experiments in space the angle is approximate and variable due to changes in flight mode, and magnitude of gravity level, on Earth and in space, as well as the particular growth speeds simulated, in units of mm/hr.

| Experiments on: | $T_{hot}$ | $T_{cold}$ | Adiabatic width | Growth speed | Angle | g |
|---|---|---|---|---|---|---|
| Earth | 500 to 760 | 30 | 9 to 14 | 6 to 1800 | 0 and 90 | 1 |
| In Space | 600 to 760 | 50 | 14 | 6.67 to 144 | 50 to 70 | $10^{-6}$ to $10^{-3}$ |
| MEPHISTO 1 simulations: | | | | | | |
| | 500 | 50 (30@1g) | 20 | 6.67 | 0 and 90 | $10^{-6}$ to 1 |
| MEPHISTO 2 simulations: | | | | | | |
| Vertical | 500 | 30 | 18 | 20.5 | 0 | $10^{-6}$ to 1 |
| Horizontal | 500 | 30 | 20 | 20.5 | 90 | $10^{-6}$ to 1 |

Table 3 Dimensionless numbers for MEPHISTO 1 and 2. For MEPHISTO 1, convection was observed at 1g, 2500 μg, and 300 μg. When the signs of the $Gr_s$ and $Gr_T$ are the same the solutal and thermal effects tend to enhance each other. $U_p$ is growth velocity in units of mm/hr.

| Dimensionless Number | MEPHISTO 1 | | MEPHISTO 2 | |
|---|---|---|---|---|
| | $U_P = 7$ | $U_P = 100$ | $U_P = 7$ | $U_P = 100$ |
| *Pr* | 0.016 | | 0.018 | |
| *Sc* | 140 | | 60 | |
| $Gr_s$ | | | | |
| 1 μg | $-1.3\times10^{-4}$ | $-4\times10^{-8}$ | 0.09 | $2.8\times10^{-5}$ |
| 300 μg | -0.04 | $-1.2\times10^{-5}$ | 27 | $8.4\times10^{-3}$ |
| 2500 μg | -0.33 | $-1.0\times10^{-4}$ | 226 | 0.07 |
| 1 g | -130 | -0.04 | $9.0\times10^{4}$ | 28 |
| $Gr_T$ | | | | |
| 1 μg | -23 | | -32 | |
| 300 μg | $-7.\times10^{3}$ | | $-9.7\times10^{3}$ | |
| 2500 μg | $-5.7\times10^{4}$ | | $-8.1\times10^{4}$ | |
| 1 g | $-2.3\times10^{7}$ | | $-3.2\times10^{7}$ | |
| Pe @ 100μg | 7 | | 20 | |

# REPORT DOCUMENTATION PAGE

*Form Approved*
*OMB No. 0704-0188*



| 1. AGENCY USE ONLY (*Leave blank*) | 2. REPORT DATE | 3. REPORT TYPE AND DATES COVERED |
|---|---|---|
| | July 1995 | Technical Memorandum |

**4. TITLE AND SUBTITLE**

Numerical Simulation of Heat and Mass Transport During Space Crystal Growth With MEPHISTO

**5. FUNDING NUMBERS**

WU–674–21–05

**6. AUTHOR(S)**

Minwu Yao, Raghu Raman, and Henry C. de Groh III

**7. PERFORMING ORGANIZATION NAME(S) AND ADDRESS(ES)**

National Aeronautics and Space Administration
Lewis Research Center
Cleveland, Ohio 44135–3191

**8. PERFORMING ORGANIZATION REPORT NUMBER**

E–9800

**9. SPONSORING/MONITORING AGENCY NAME(S) AND ADDRESS(ES)**

National Aeronautics and Space Administration
Washington, D.C. 20546–0001

**10. SPONSORING/MONITORING AGENCY REPORT NUMBER**

NASA TM–107015

**11. SUPPLEMENTARY NOTES**

Minwu Yao, Ohio Aerospace Institute, 22800 Cedar Point Road, Cleveland, Ohio 44142; Raghu Raman, University of Florida, Gainesville, Florida 32611; and Henry C. de Groh III, NASA Lewis Research Center. Responsible person, Henry C. de Groh III, organization code 5110, (216) 433–5025.

**12a. DISTRIBUTION/AVAILABILITY STATEMENT**

Unclassified - Unlimited
Subject Category 29

This publication is available from the NASA Center for Aerospace Information, (301) 621–0390.

**12b. DISTRIBUTION CODE**

**13. ABSTRACT** ***(Maximum 200 words)***

The MEPHISTO space experiments are collaborative United States and French investigations aimed at understanding the fundamentals of crystal growth. Microgravity experiments were conducted aboard the USMP–1 and –2 missions on STS–52 and 62 in October 1992 and March 1994 respectively. MEPHISTO is a French designed and built Bridgman type furnace which uses the Seebeck technique to monitor the solid/liquid interface temperature and Peltier pulsing to mark the location and shape of the solid/liquid interface. In this paper the Bridgman growth of Sn-Bi and Bi-Sn under terrestrial and microgravity conditions is modeled using the finite element code, FIDAP. The numerical model considers fully coupled heat and mass transport, fluid motion and solid/liquid phase changes in the crystal growth process. The primary goals of this work are: to provide a quantitative study of the thermal buoyancy-induced convection in the melt for the two flight experiments; to compare the vertical and horizontal growth configurations and systematically evaluate the effects of the various gravity levels on the solute segregation. Numerical results of the vertical and horizontal Bridgman growth configurations are presented.

**14. SUBJECT TERMS**

Bismuth; Tin; Sn; Bi; Bi-Sn; Solidification; Bridgman growth; MEPHISTO; Convection; Interface

**15. NUMBER OF PAGES**

30

**16. PRICE CODE**

A03

| 17. SECURITY CLASSIFICATION OF REPORT | 18. SECURITY CLASSIFICATION OF THIS PAGE | 19. SECURITY CLASSIFICATION OF ABSTRACT | 20. LIMITATION OF ABSTRACT |
|---|---|---|---|
| Unclassified | Unclassified | Unclassified | |